Towards Long-Wavelength Ionospheric Correction of InSAR Time Series Using GNSS-Based TEC

Yidi Wang, *Student Member, IEEE*, Zhang Yunjun, *Member, IEEE*, Ningbo Wang, Runqing Liu, Cunren Liang, Yosuke Aoki, *Member, IEEE*, and Robert Wang, *Senior Member, IEEE*

***Abstract*—Ionospheric delays dominate the long-wavelength deformation measurement errors in interferometric synthetic aperture radar (InSAR) time series. Most existing correction techniques are SAR data-based and rely on interferometric coherence, which restricts their applicability in vegetated areas and operational systems. Here, we investigate a rapid ionospheric correction approach that uses external total electron content (TEC) products derived from global navigation satellite system (GNSS) observations with a focus on the long-wavelength deformation mapping. We tested five products, including global ionospheric maps (GIMs), Madrigal TEC products, and local ionospheric maps. The method is fully automatic and reduces processing time from days to minutes, desirable for operational data systems as well as existing InSAR databases. We validate the method using C-band Sentinel-1 and L-band ALOS-2 data in the western United States, northern Chile, and southwestern Japan. Using independent GNSS displacements as reference, our method reduces the RMSE from 1.7–3.8 to 0.9–2.9 mm/yr for Sentinel-1 ascending tracks in mid-latitude regions and all descending tracks, achieving accuracy comparable to the split-spectrum method (1.0–2.8 mm/yr). However, for Sentinel-1 ascending track in low-latitude regions and ALOS-2 descending tracks, the split-spectrum method still remains much more precise. We demonstrate the effectiveness of the GNSS-based TEC approach using OPERA displacement products over the western USA. The global analysis of ionospheric delays using multiyear GIM products could serve as a useful reference for potential ionospheric impact on InSAR velocities for most common InSAR missions.**

***Index Terms*—Global navigation satellite system (GNSS)-based total electron content (TEC) product, interferometric synthetic aperture radar (InSAR), ionospheric correction, long-wavelength deformation velocity.**

I. INTRODUCTION

TIME series interferometric synthetic aperture radar (InSAR) is a powerful imaging technique to measure the subtle surface deformation [1] caused by surface and subsurface processes such as earthquakes [2], volcanic activities [3], landslides [4], ecosystem [5], and anthropogenic activities [6]. However, its accuracy is limited by decorrelation, unwrapping errors, and atmospheric propagation delays [7], [8]. Ionosphere, which is the upper atmosphere with altitudes of approximately 50–1000 km, is formed by ionized particles from atmospheric atoms and molecules due to solar radiation. The content of these charged particles is usually represented by the ionospheric total electron content (TEC) [9], which varies by location, time of day, season, and geomagnetic and solar activities [10]. The solar activity has a ~11 year cycle. The ionospheric delay is the dominant error source for the long spatial wavelength deformation mapping [11], [12].

There are mainly five categories of ionospheric delay estimation or correction methods. The first category utilizes the Faraday rotation effect that occurs when a linearly polarized wave passes through the ionosphere [13], [14]. These methods are suitable for full-polarimetric SAR, such as those from the BIOMASS mission [15]. The second category utilizes the range group-phase delay difference due to the dispersive ionosphere, which is equal in magnitude but opposite in sign [16]. Its accuracy depends on the precision of speckle tracking, which is used to estimate the range delay from SAR amplitude [17]. The third category uses the multiple-aperture interferometry to estimate the azimuth shift caused by the ionosphere [18]. It shows effectiveness in small-scale ionospheric delay [19]. However, this method cannot distinguish between deformation in the azimuth direction and ionospheric effect, limiting its applicability to areas without deformation in the azimuth direction.

The fourth category uses the range split-spectrum technique, which splits the range spectrum into two sub-bands and separates the dispersive ionosphere from other nondispersive components [20], [21]. The accuracy of this method is limited by the SAR range bandwidth [22] and interferometric coherence. It has proven to be the most precise method among the above four for SAR systems with range bandwidths of 28 MHz and above [23] and is currently the most widely used method [24], [25], [26]. However, this method requires band splitting and phase unwrapping, which can be computationally expensive and difficult in low-coherent areas due to dense vegetation.

The fifth category uses the external ionospheric TEC products, which are usually estimated from the dual-frequency

Received 26 September 2025; revised 3 December 2025; accepted 17 January 2026. Date of publication 21 January 2026; date of current version 10 February 2026. This work was supported in part by the Innovative Research Groups of the National Natural Science Foundation of China under Grant 62421001. *(Corresponding author: Zhang Yunjun.)*

Yidi Wang, Zhang Yunjun, and Robert Wang are with the National Key Laboratory of Microwave Imaging, Aerospace Information Research Institute, Chinese Academy of Sciences, Beijing 100190, China, and also with the School of Electronic, Electrical and Communication Engineering, University of Chinese Academy of Sciences, Beijing 100049, China (e-mail: wangyidi23@mails.ucas.ac.cn; yunjunz@aircas.ac.cn; yuwang@mail.ie.ac.cn).

Ningbo Wang and Runqing Liu are with the Aerospace Information Research Institute, Chinese Academy of Sciences, Beijing 100094, China, and also with the School of Electronic, Electrical and Communication Engineering, University of Chinese Academy of Sciences, Beijing 100049, China.

Cunren Liang is with the Institute of Remote Sensing and Geographic Information System, School of Earth and Space Sciences, Peking University, Beijing 100871, China.

Yosuke Aoki is with the Earthquake Research Institute, The University of Tokyo, Tokyo 113-0032, Japan.

This article has supplementary downloadable material available at https://doi.org/10.1109/TGRS.2026.3656511, provided by the authors.

Digital Object Identifier 10.1109/TGRS.2026.3656511

global navigation satellite system (GNSS) network [27]. This method is fast and independent of InSAR coherence, thus, it is desired for emergency response with big data and operational data systems such as the European ground motion service (EGMS) [28], the observational products for end-users from remote sensing analysis (OPERA) displacement [29], the looking into the continents from space with synthetic aperture radar (LiCSAR) [30], and the Advanced Rapid Imaging and Analysis (ARIA) Center for Natural Hazards project [31]. Previous attempts have been pursued to estimate ionospheric delay from either regional GNSS network [32] or International GNSS Service (IGS) TEC products [33], [34] and apply it to a few interferograms, both estimations show agreement with independent GNSS or split-spectrum estimations to the first order but with underestimated magnitude [24]. However, the IGS global ionospheric maps (GIMs) have proven to be accurate enough in terms of absolute accuracy for stack coregistration of C-band Sentinel-1 [35] and used in the OPERA coregistered single look complex (CSLC) product generation [36], [37]. Therefore, it is of interest to evaluate the external TEC-based ionospheric correction in InSAR time series in terms of relative accuracy.

Moreover, GNSS-based ionospheric TEC estimation has made several significant advances in recent years. Compared with IGS GIMs, which are produced using 200–400 globally distributed GNSS stations with gaps filled using climatological models and smoothed in time using Kalman filtering [33], [34], the Massachusetts Institute of Technology (MIT) Haystack Observatory collects and processes TEC data from more than 9000 ground GNSS stations with products available on the Madrigal database [38], [39]. The larger number of stations and less smoothing of the Madrigal TEC product [40] lead to higher temporal and spatial resolutions with mesoscale (100–1000 km) structures preserved [41], which is desired for spaceborne InSAR observation with typical swaths of 50–250 km. Using observations from ~40 000 000 phones, Google has demonstrated ionospheric TEC estimations with even higher spatial and temporal resolutions and coverage compared with the Madrigal TEC [42]. It is of interest to evaluate these new TEC products for InSAR ionospheric delay correction.

Here, we integrate various GNSS-based TEC products into the routine InSAR time series analysis workflow for ionospheric correction with focus on the long wavelength phase component. Using the range split-spectrum estimation and independent GNSS observation as references, we evaluate the relative accuracy of these GNSS-based TEC products and their applicability for long spatial wavelength deformation mapping using both C-band and L-band SAR.

In what follows, we briefly describe the ionospheric delay calculation procedure and several GNSS-based TEC products (see Section II), present the real data experiments of C-/L-band SAR in three test sites with different levels of ionospheric TEC (see Section III), followed by discussions of results (see Section IV) and conclusion (see Section V).

II. METHODOLOGY

We briefly describe here the ionospheric delay calculation procedure using three types of GNSS-based TEC products.

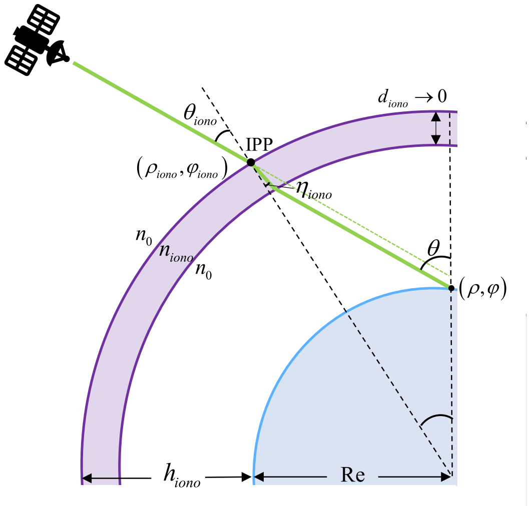

Fig. 1. Ionospheric mapping geometry of GNSS-based TEC. Purple band represents the ionosphere with a depth of d_{iono}. Re is the Earth radius, IPP is the ionospheric piercing point. θ and θ_{iono} are the incidence angle of the radar LOS vector on the ground and at IPP, and η_{iono} is the refraction angle of the radar LOS vector at IPP.

A. Ionospheric Delay Estimation From GNSS-Based TEC

The ionosphere introduces a phase advance and group delay in the radar signal that passes through. The geometry is shown in Fig. 1. Under the first-order assumption, this absolute single-path phase delay along the radar line-of-sight (LOS) direction can be expressed as [43]

$$r_{\text{iono}} = \text{TEC} \cdot K / f_0^2 \tag{1}$$

where $K = 40.31\text{m}^3/\text{s}^2$ is a constant, f_0 is the radar carrier frequency in hertz, and TEC is the number of free electrons per unit area along the slant range in the radar LOS direction in the unit of TECU with $1\text{TECU} = 10^{16}\text{electrons/m}^2$.

The slant TEC can be calculated from the vertical TEC (VTEC) following the widely used effective ionospheric thin-shell assumption [44] as

$$\text{TEC} = \frac{\text{VTEC}\left(\rho_{\text{iono}}, \varphi_{\text{iono}}\right)}{\cos\left(\eta_{\text{iono}}\right)} \tag{2}$$

where $\text{VTEC}(\rho_{\text{iono}}, \varphi_{\text{iono}})$ is the VTEC at the ionospheric piercing point (IPP) with $(\rho_{\text{iono}}, \varphi_{\text{iono}})$ as the latitude and longitude, which can be obtained from GNSS-based TEC products. η_{iono} is the refraction angle of the LOS vector at IPP and can be calculated following the Snell's law as [35]

$$\eta_{\text{iono}} = \arcsin\left(\frac{n_0}{n_{\text{iono}}} \sin\left(\theta_{\text{iono}}\right)\right) \tag{3}$$

where $n_0 = 1$ and n_{iono} are the refractive index of vacuum and ionosphere, respectively, θ_{iono} is the incident angle of the LOS vector at IPP, which can be calculated from the incidence angle of the LOS vector on the ground θ as [45]

$$\theta_{\text{iono}} = \arcsin\left(\frac{\text{Re} \cdot \sin\theta}{\text{Re} + h_{\text{iono}}}\right) \tag{4}$$

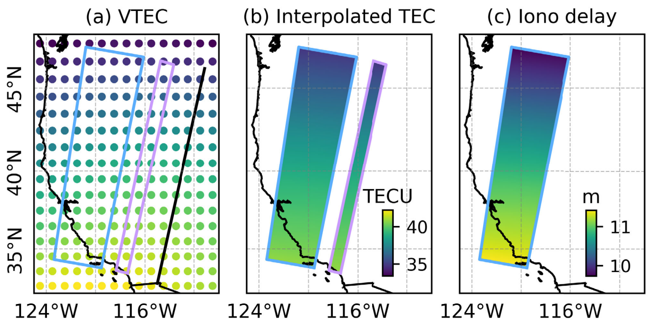

Fig. 2. Ionospheric delay calculation procedure from GNSS-based TEC products. (a) GNSS-based vertical TEC from JPL high-resolution GIM on February 20, 2015, over the western USA. Blue box presents the footprint of the SAR image from ALOS-2 descending track 168 frame 2700–2900, purple box represents the projected footprint of the SAR image at IPP, and black line represents the ground track of the SAR satellite. (b) Slant TEC along the radar LOS direction interpolated from (a) at IPP (purple box) following equation (2), which is then resampled to the ground (blue box). (c) Absolute ionospheric delay estimated from the blue box in (b) following equation (1).

TABLE I

SUMMARY OF SPATIAL AND TEMPORAL RESOLUTIONS OF THE USED GNSS-BASED TEC PRODUCTS

TEC products	Spatial resolution [lat × lon]	Temporal resolution
GIM-JPL[1]	2.5° × 5°	2-hour
GIM-CAS[1]	2.5° × 5°	30-min
GIM-JPLD[2]	1° × 1°	15-min
Madrigal[3]	1° × 1°	5-min
LIM	1° × 1°	15-min

[1] https://cddis.nasa.gov/archive/gnss/products/ionex/
[2] https://sideshow.jpl.nasa.gov/pub/iono_daily/gim_for_research/jpld/
[3] http://cedar.openmadrigal.org/

where Re is the radius of the earth, and h_{iono} is the approximate thin-shell height of the ionosphere (~450 km). n_{iono} is a function of VTEC and can be calculated as [43]

$$n_{\text{iono}} = 1 + \frac{\text{VTEC}\left(\rho_{\text{iono}}, \varphi_{\text{iono}}\right) \cdot K}{f_0^2} \tag{5}$$

To derive the VTEC$(\rho_{\text{iono}}, \varphi_{\text{iono}}, t)$ from the standard GNSS-based TEC products, we use a 2-D spatial interpolation and 1-D temporal interpolation, which considers the impact of the Earth's rotation [46]. The procedure is shown in Fig. 2. $(\rho_{\text{iono}}, \varphi_{\text{iono}})$ (purple box in Fig. 2) can be calculated from the coordinate of the ground target (ρ, φ) (blue box in Fig. 2) using the precise geodetic formula or spherical distance formula [35].

B. Overview of GNSS-Based TEC Products

We test three types of VTEC products generated from GNSS observations: GIMs from IGS centers, the Madrigal TEC product from MIT and a local ionospheric map (LIM) from the Chinese Academy of Sciences. The spatial and temporal resolutions of these products are summarized in Table I with an example shown in Fig. 3.

1) Global Ionospheric Maps: GIM provides global-scale VTEC products and is routinely generated by several IGS-associated analysis centers [47]. We use GIM products from two centers: the Chinese Academy of Sciences (CAS), which has a 30-min temporal resolution [48], and the Jet Propulsion Laboratory (JPL), which has a 2-h temporal resolution [33]. Both have a spatial resolution of 2.5° (latitude) ×5° (longitude).

We also use the newly released high-resolution JPL GIM, the JPLD data product, which has a high spatiotemporal resolution of 15 min (time) ×1° (latitude) ×1° (longitude) [49], [50]. Both GIM-JPL and GIM-JPLD products are based on observations from approximately 200–400 GNSS stations using signals from GPS, GLONASS, and later on Galileo satellites. The GIM-JPL product uses a single-shell ionospheric mapping model, while the GIM-JPLD product uses a three-shell ionospheric mapping model, which could further mitigate the systematic errors in the VTEC maps [50].

2) Madrigal TEC Product: The MIT Haystack Observatory generates VTEC maps using observational data from approximately 9000 GNSS stations worldwide [40], using a strictly data-driven approach, without underlying models to smooth out gradients in TEC [38]. Since June 2005, the resulting TEC data have been incorporated into the Madrigal open-source database system, which provides high spatiotemporal resolution of 5 min (time) ×1° (latitude) ×1° (longitude).

In subsequent ionospheric correction, we apply a 2-D discrete convolution to the VTEC maps to reduce the impact of potentially inaccurate short wavelength TEC variation (see Fig. 4)

$$\overline{\text{VTEC}} = \mathbf{h} * \text{VTEC} \tag{6}$$

where $\overline{\text{VTEC}}$ is the filtered VTEC, $\mathbf{h}$ is a 2-D mean-value convolution kernel, i.e., an all-ones matrix. For each study area, we choose VTEC data within a 10° expanded range, and filter it using a 5 × 5 size kernel [see Fig. 4(b)].

Due to the used data-driven approach, the Madrigal TEC products have gaps in their spatial coverage, such as in most of Africa and Asia, which is about half of the global land and most oceanic regions [see Fig. 3(c)]. Several attempts have been pursued to fill these gaps by combining with GIM products and using machine learning approaches [41].

3) Local Ionospheric Map: We also tried the LIM generated using observation data from over 300 GNSS stations, confined to each of the study areas. Observation data are primarily obtained from the IGS and the University Navigation Satellite Timing and Ranging (NAVSTAR) Consortium and processed in receiver independent exchange (RINEX) format [51], [52]. The LOS ionospheric information is retrieved through precise point positioning with ambiguity resolution (PPPAR) approach [53], which exhibits high accuracy and low noise level compared to the conventional carrier-to-code leveling technique. Slant TEC values are first derived from the station data and converted to VTEC by assuming a thin ionospheric shell at 450 km altitude [54], [55]. A grid with resolution of 1° × 1° in latitude and longitude is defined, and VTEC values are interpolated using inverse distance weighting (IDW) interpolation. To minimize noise and enhance the smoothness of the interpolated results, a Gaussian filter with a 3 × 3 kernel size and a standard deviation of 1 TECU is applied.

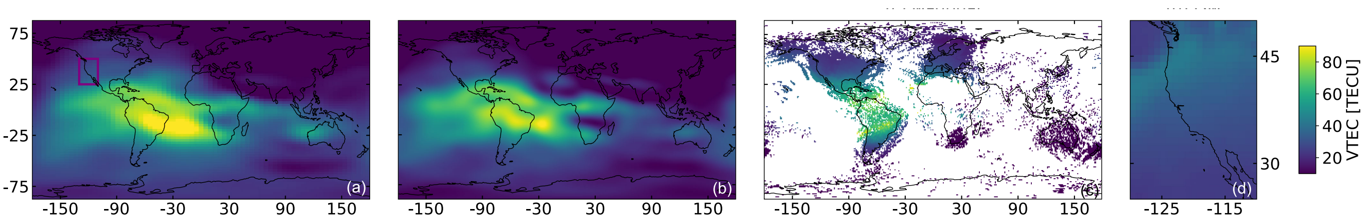

Fig. 3. Different GNSS-based TEC products at 06 UTC on May 05, 2023. The purple box in (a) represents the regional range of the LIM in (d). (a) GIM-JPL. (b) GIM-JPLD. (c) Madrigal. (d) LIM.

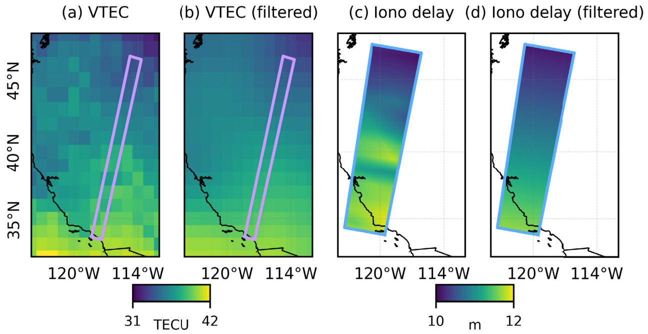

Fig. 4. Filtering process of Madrigal TEC products. (a) Madrigal TEC at 20 UTC on February 20, 2015, in the western USA. The purple box represents the projected footprint of the SAR image at IPP. (b) Madrigal TEC product after filtering. (c)–(d) Absolute ionospheric delay estimated from (a) and (b), respectively. Blue box presents the footprint of the SAR image on the ground.

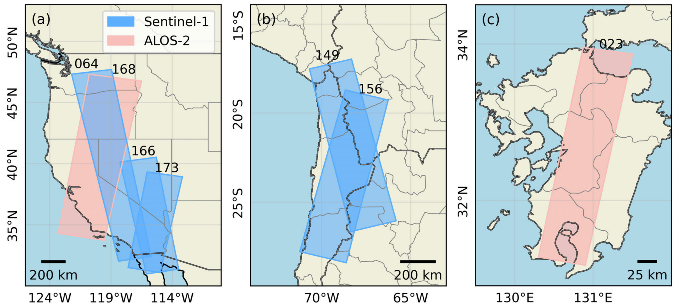

Fig. 5. Study areas with data coverage in (a) western USA, (b) northern Chile, and (c) southwest Japan.

III. EXPERIMENTAL RESULTS

We evaluate the performance of ionospheric correction with GNSS-based TEC products in three study areas with various ionospheric states, including western USA, northern Chile, and southwest Japan (see Fig. 5). We compare the ionospheric correction with the well-established range split-spectrum technique and assess the long spatial wavelength deformation accuracy using independent GNSS displacement as reference. The detailed dataset information is summarized in Table II, including 11 358 scenes of Sentinel-1 imagery, and 150 and 190 scenes of ALOS-2 ScanSAR and StripMap mode imagery, respectively.

We use the topsStack [22] and alosStack [59] processors in ISCE-2 software [60] to coregister the stacks of Sentinel-1 and ALOS-2 SLCs. More specifically, we first perform the geometric coregistration using precise orbits and shuttle radar topography mission (SRTM) digital elevation model (DEM) [61] (SRTMGL1, 1 arc second with void-filled, ~30 m), then apply the enhanced spectral diversity and cross correlation techniques for the refined coregistration. For Sentinel-1 data, we generate interferograms with the nearest ten sequential connections, multilook with 30 and 10 looks in the range and azimuth directions, respectively, and apply the Goldstein filtering with a strength of 0.2. For ALOS-2 ScanSAR data, we generate interferograms with a full-connection network, i.e., all possible pairs, multilook with 10 and 56 looks in the range and azimuth directions. For ALOS-2 StripMap data, we generate interferograms with the nearest ten sequential connections, multilook 60 and 90 looks in the range and azimuth directions, and apply the Goldstein filtering with a strength of 0.5. For both Sentinel-1 and ALOS-2, we unwrap the interferogram using the minimum cost flow method via statistical-cost, network-flow algorithm for phase unwrapping (SNAPHU) [62]. For comparison purposes, we also apply the range split-spectrum technique in topsStack [26] and alosStack [25] to derive the ionospheric delay time series.

TABLE II

SUMMARY OF USED SAR DATASETS

Sensor	Track number	Imaging mode	Start / end date	# of acquisitions / interferograms
S1_A	064	TOPS	2015-03-27 / 2024-04-08	206 / 2005
S1_A	166	TOPS	2015-04-03 / 2021-12-21	162 / 1565
S1_D	173	TOPS	2015-06-14 / 2024-03-22	285 / 2795
S1_A	149	TOPS	2014-10-27 / 2024-03-20	324 / 3185
S1_D	156	TOPS	2014-10-16 / 2024-03-21	238 / 2325
A2_D	168	ScanSAR	2015-02-20 / 2022-09-09	32 / 496
A2_D	023	StripMap	2015-02-23 / 2019-04-01	38 / 325

We perform the time series analysis using the small baseline approach from the MintPy software [8]. More specifically, we correct for troposphere using the ERA5 weather reanalysis data [63] via PyAPS [64], topographic residuals due to DEM errors [65], and solid Earth tides via PySolid [35], [66]. We correct for ionosphere using the GNSS-based TEC product as described in Section II. To preserve the long spatial wavelength phase contributions, which are our signal of interest, we do not apply phase deramping nor correct for the orbital error. The potential contribution of the orbital error is calculated in Supplementary Materials Section S2 and discussed in Section III-C.

We validate the final InSAR displacement time series using the independent GNSS displacement from the University of

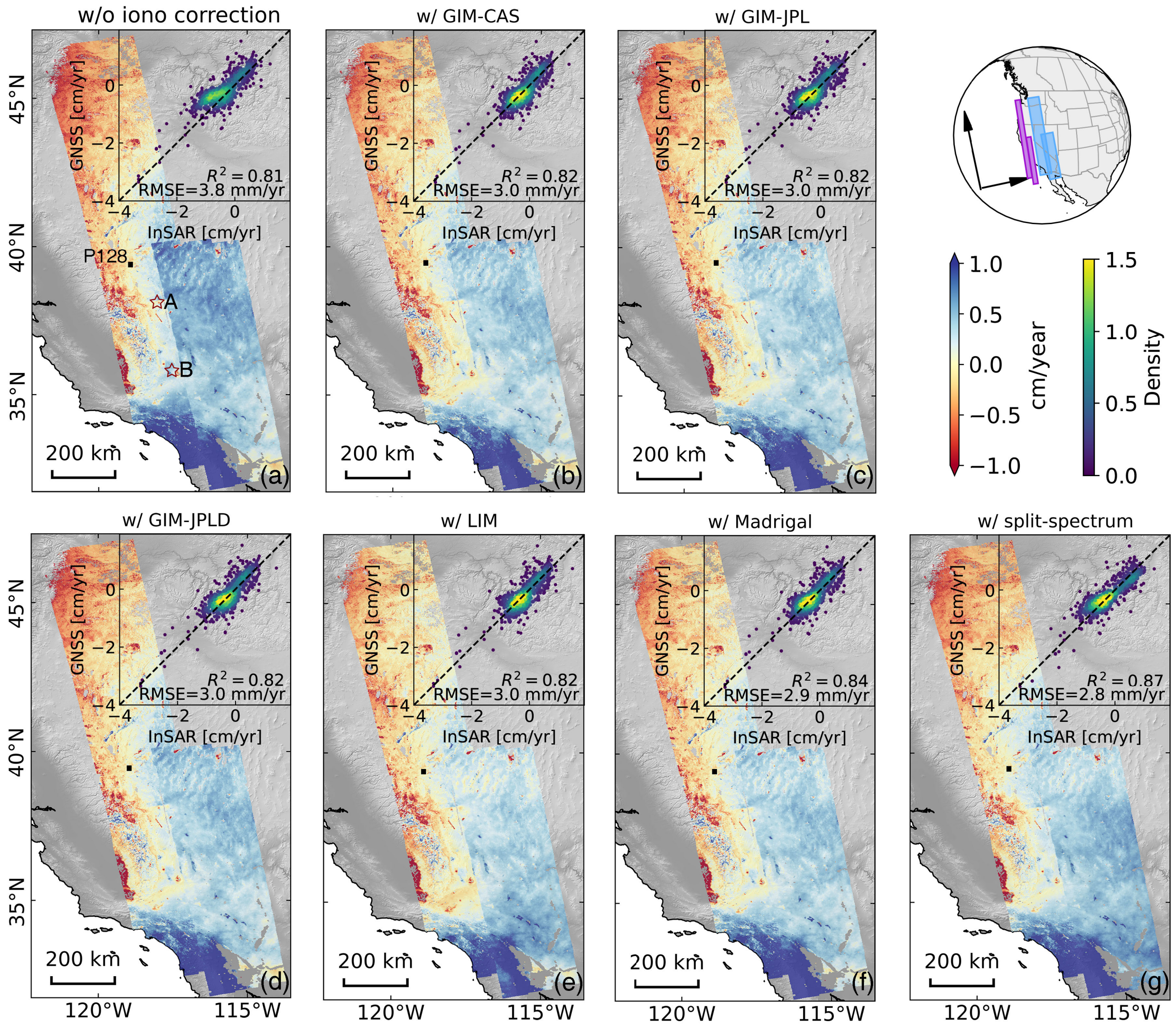

Fig. 6. InSAR LOS velocity in western USA from Sentinel-1 ascending tracks 064 (2015–2024) and track 166 (2015–2021). (a)–(g) Deformation velocity (a) without ionospheric correction, (b)–(g) with ionospheric correction using GIM-CAS, GIM-JPL, GIM-JPLD, LIM, Madrigal TEC products, and the range split-spectrum method, respectively. The black square represents the reference point (GNSS station: P128). Scatter plot in the upper right corner of each subplot shows the comparison between InSAR and 1278 independent GNSS velocities. Circular map on the upper right shows the dataset location, with the blue box for the ground and the purple box for the IPP. Two red empty stars in (a) represent (A) 2020 Monte Cristo Range earthquake [56] and (B) 2019 Ridgecrest earthquakes [57], respectively. The impact of the coseismic deformation from these earthquakes is estimated and removed using a Heaviside step function during the linear velocity estimation with details as shown in Figs. S11 and S12.

Nevada at Reno (UNR) [67] as reference, and evaluate the ionospheric correction accuracy from various GNSS-based TEC products. Since the InSAR reference frame is determined by its orbit [11], which is ITRF2014 for both Sentinel-1 [68] and ALOS-2 [69], we use the GNSS solutions from UNR in ITRF2014 for consistency, therefore, we do not need to remove the impact of the plate rotation for this comparison purpose [11], [12]. We select GNSS observations that overlap with the InSAR data in both time and space, then project the 3-D displacements in the east, north, and vertical directions into the InSAR LOS direction, to obtain the GNSS LOS displacement time series. Then, we estimate a linear velocity for each GNSS station and InSAR pixel, and a Heaviside step function for each earthquake to account for the coseismic deformation, from its displacement time series. Next, for both InSAR and GNSS datasets, we choose a common spatial reference at a GNSS station for each InSAR track, except for Sentinel-1 ascending track 149 in northern Chile, where a median difference between GNSS and InSAR velocities is estimated and removed from all GNSS velocities. Last, we obtain the InSAR velocity at each GNSS station using a linear interpolation [8], and calculate the root mean square error (RMSE) and the coefficient of determination R^2 between InSAR and GNSS (see Supplementary Materials Section S3 for the detailed procedure). RMSE is calculated as

$$\mathrm{RMSE} = \sqrt{\frac{1}{N-1}\|\mathbf{v}_{\mathrm{GNSS}} - \mathbf{v}_{\mathrm{InSAR}}\|^2} \tag{7}$$

where $\mathbf{v}_{\mathrm{GNSS}}, \mathbf{v}_{\mathrm{InSAR}} \in \mathbb{R}^N$ are the GNSS and InSAR velocity vectors at N GNSS stations. $\|\cdot\|$ denotes the Euclidean norm.

R^2 is calculated as

$$R^2 = 1 - \frac{\|\mathbf{v}_{\text{GNSS}} - \mathbf{v}_{\text{InSAR}}\|^2}{\|\mathbf{v}_{\text{GNSS}} - \bar{v}_{\text{GNSS}}\|^2} \tag{8}$$

where $\bar{v}_{\text{GNSS}}$ is the mean value of all GNSS velocities.

A. C-Band Sentinel-1 in United States and Chile

Fig. 6 shows the deformation velocity measured by InSAR for Sentinel-1 ascending tracks 064 and 166 in the western USA. We calculate the median value of the overlapping areas between the two tracks and subtract it to enable the stitching of the tracks. All GNSS-based TEC methods improve the accuracy of InSAR-derived velocity, reduce the RMSE between GNSS and InSAR from 3.8 to 2.9–3.0 mm/yr, which corresponds to a 21%–24% improvement. The range split-spectrum method achieves the smallest RMSE of 2.8 mm/yr, while our proposed method yields comparable results. Among these GNSS-based TEC products, Madrigal performs slightly better than the others.

Fig. 7(a)–(c) shows the result of Sentinel-1 descending track 173 in the mid-latitude region of western USA. The data are acquired at approximately 6 A.M. local solar time when ionospheric TEC levels are weak. Using GNSS station P625 as a reference, the RMSE improves from 1.7 to 1.5 mm/yr after applying Madrigal TEC product, representing a 12% reduction. The range split-spectrum method reduces the RMSE to 1.4 mm/yr. Fig. 7(d)–(f) shows the result of Sentinel-1 descending track 156 in the low-latitude region of northern Chile, where the circles denote GNSS stations. Using GNSS station SOCM as the reference point, after correction using Madrigal TEC products, the RMSE between InSAR and GNSS velocity is improved from 2.1 to 0.9 mm/yr, representing a 57% improvement. The range split-spectrum method achieved a corrected RMSE of 1.0 mm/yr.

Fig. 7(g)–(i) shows the deformation velocity measured by Sentinel-1 ascending track 149 in northern Chile. In this analysis, we remove the median values of both InSAR and GNSS velocity to mitigate the effect of reference point selection on relative InSAR measurements. More specifically, this step is used because the spatial distribution of GNSS stations is uneven, with only 19 stations in the study area meeting the evaluation criteria, and the velocity fields generated using different correction methods exhibit spatial discrepancies. The RMSE between InSAR and GNSS velocity decreases from 2.6 to 2.5 mm/yr, while the R^2 increases from 0.75 to 0.86 when using the range split-spectrum method. However, the performance of our proposed correction method is less favorable: after applying Madrigal TEC products, the RMSE increases from 2.6 to 3.4 mm/yr, while R^2 decreases from 0.75 to 0.63. This reduced performance is related to the radar acquisition time, which occurs around 6 P.M. local solar time and coincides with strong ionospheric activity. The accuracy of current GNSS-based TEC products is insufficient to resolve the associated spatial gradients.

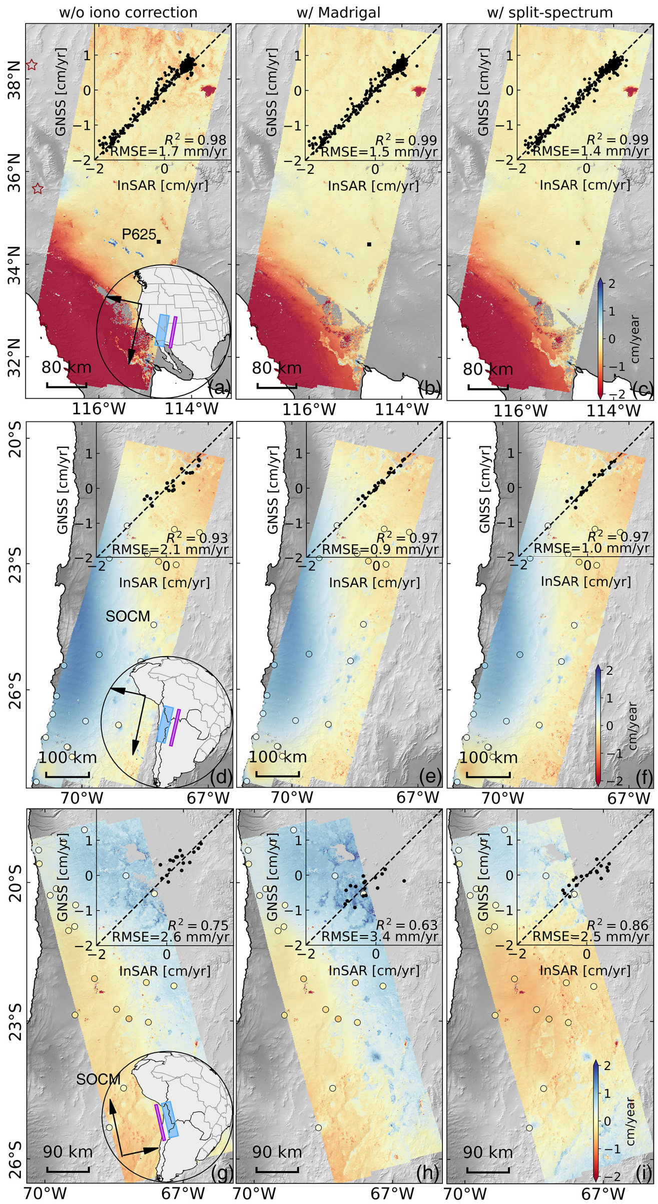

Fig. 7. Deformation velocity measured by InSAR in LOS direction for three Sentinel-1 orbits. Similar to Fig. 6, (left) shows the deformation velocity without ionospheric correction, (central) with ionospheric correction using Madrigal TEC products, and (right) using the range split-spectrum method. (a)–(c) Results of Sentinel-1 descending track 173 (2015–2024) in western USA. The black square represents reference point (GNSS station: P625). R^2 and RMSE are computed from 282 GNSS stations. Two red empty stars in (a) represent the 2019 Ridgecrest earthquakes (to the south) and the 2020 Monte Cristo Range earthquake (to the north), respectively. (d)–(f) Similar to (a)–(c) but for Sentinel-1 descending track 156 (2014–2024) in northern Chile with circles denote the 20 GNSS stations and reference point in GNSS station SOCM. (g)–(i) Similar to (d)–(f) but for Sentinel-1 ascending track 149 (2014–2024) with 19 GNSS stations and reference point in GNSS station SOCM.

B. L-Band ALOS-2 in United States and Japan

Since the ionospheric delay effect is proportional to the square of the wavelength, the ionospheric effect in the L-band is approximately 17 times that in the C-band [35]. In this study, we experiment with ALOS-2 descending orbit data in western USA [see Fig. 8(a)–(c), track 168] and southwest Japan [see Fig. 8(d)–(f), track 023], and found that the spatial gradient accuracy of current GNSS-based products did not improve the InSAR long wavelength deformation mapping. In the western USA region, the range split-spectrum method reduces the RMSE between InSAR and GNSS velocity from 28.4 to 2.8 mm/yr; while all GNSS-based TEC products lead

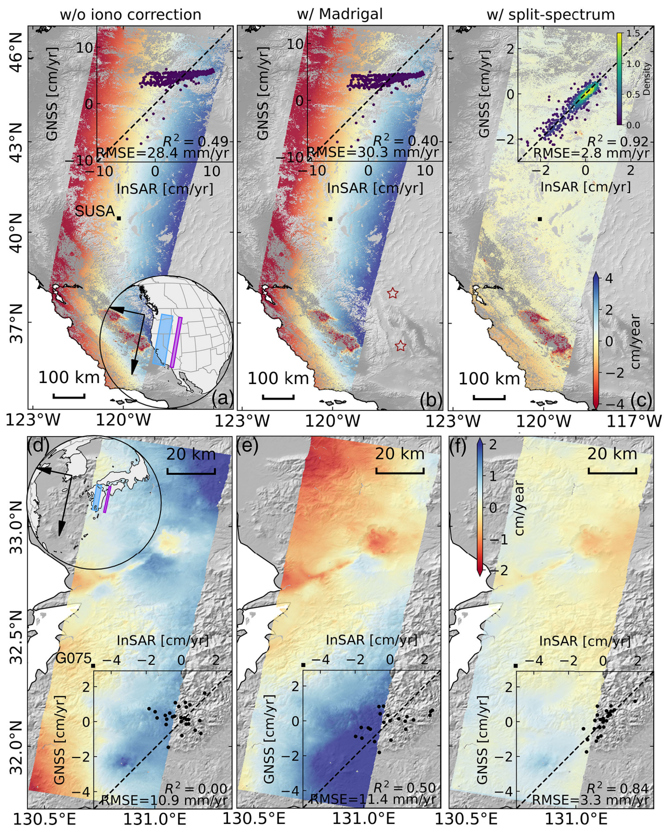

Fig. 8. Similar to Fig. 7 but for two ALOS-2 descending orbits. (a)–(c) Results of ALOS-2 ScanSAR descending track 168 (2015–2022) in western USA with 567 GNSS stations and reference point in GNSS station SUSA. (d)–(f) Results of ALOS-2 StripMap descending track 023 (2015–2019) in western Japan with 22 GNSS stations and reference point in GNSS station G075. The impact of the coseismic deformation from the 2016 Kumamoto earthquake [58] is estimated and removed using a Heaviside step function as shown in Fig. S13.

to a slight RMSE increase from 28.4 to 29.7–36.2 mm/yr. In the southwest Japan region, the range split-spectrum method improves the RMSE from 10.9 to 3.3 mm/yr; while all GNSS-based TEC products also lead to a slight RMSE increase from 10.9 to 11.0–12.0 mm/yr. In conclusion, for L-band SAR, the GNSS-based TEC approach does not work well, and the range split-spectrum method remains as the favorable method.

C. Statistical Summary on the Accuracy of Ionospheric Corrections

We summarize the statistical results from all tested methods and datasets in Fig. 9. For all C-band Sentinel-1 datasets, except for the ascending orbit in northern Chile (track 149), the ionospheric correction method proposed in this study effectively improves the accuracy of InSAR measurements for long-wavelength deformation. For all L-band ALOS-2 data, the range split-spectrum method remains as the only working approach. Among these methods, TEC products data with high resolution exhibit greater advantages than those with low resolution: the Madrigal TEC products exhibit better performance than the other TEC products.

The residual discrepancy between GNSS and InSAR (after correction with the range split-spectrum method, as shown in Fig. 9(a) last column) contains contributions from residual tropospheric delays, orbital errors, and GNSS displacement uncertainties. The contribution of orbital errors for each of the used InSAR time series is estimated following Fattahi and Amelung [70] and shown in Supplementary Materials Section S2. Based on the orbit accuracy of Sentinel-1 [68] and ALOS-2 [69], the orbital error could contribute an apparent velocity of 0.12–0.19 mm/year for Sentinel-1, and of 0.38–7.99 mm/year for ALOS-2, the later is significantly larger than the estimated RMSE of 2.8 mm/year, indicating an underestimated orbital accuracy of ALOS-2. In spite of the much higher sensitivity to the ionospheric delay, the RMSE of L-band ALOS-2 descending track (~12 P.M. local solar time; 2.8–3.3 mm/year) is in the same level as the C-band Sentinel-1 ascending track (~6 P.M. local solar time; 2.5–2.8 mm/year); therefore, we argue that no significant residual ionospheric delays remain in the InSAR result after range split-spectrum correction.

We further summarize and simplify our results into Fig. 10: for C-band Sentinel-1 data, the GNSS-based TEC correction works for most weak ionospheric states, i.e., most descending tracks, and ascending track in mid-latitude regions, but does not work for strong ionospheric states, such as those in the equatorial ionization anomaly crests and trough; while for L-band ALOS-2 data, the GNSS-based TEC correction does not work yet due to the higher sensitivity of L-band SAR and not accurate enough mesoscale ionospheric features in the current TEC products.

D. Computational Efficiency and Run Time

Our method is fast in computation. Taking the Sentinel-1 ascending track 166 (1235 SLC images with 162 acquisitions) as an example, using a computing server equipped with one Intel[1] Xeon Platinum 8260 CPU with 2.40 GHz, our method takes ~4 s to download one GNSS-based TEC product on average and ~10 min to download all 162 global GNSS-based TEC products, and ~6 min to estimate the ionospheric delay time series, including the data reading, filtering, computation, and writing. While the range split-spectrum method requires ~24 days to generate 480 ionospheric delay interferometric pairs and ~8 min to invert for the ionospheric delay time series.

IV. DISCUSSION

A. Inaccurate Range Split-Spectrum Estimation Examples

Although the range split-spectrum method can generally achieve high accuracy in ionospheric delay estimation, its practical application is fundamentally constrained by coherence-related challenges. Fig. 11(a)–(c) illustrates three representative cases of erroneous ionospheric phase estimation. In the first two cases, severe decorrelation over water bodies and vegetated areas, compounded by the additional coherence loss induced by frequency separation, leads to phase unwrapping errors and inaccurate ionospheric delay estimates [see Fig. 11(a) and (b)]. These two types of errors have been previously reported in [21].

In the third case, the ionospheric phase appears visually consistent [see Fig. 11(c)], but the error primarily originates from strong decorrelation at the interferogram boundaries [see Fig. 11(d)]. Excluding such estimates significantly alters the

---

[1] Registered trademark.

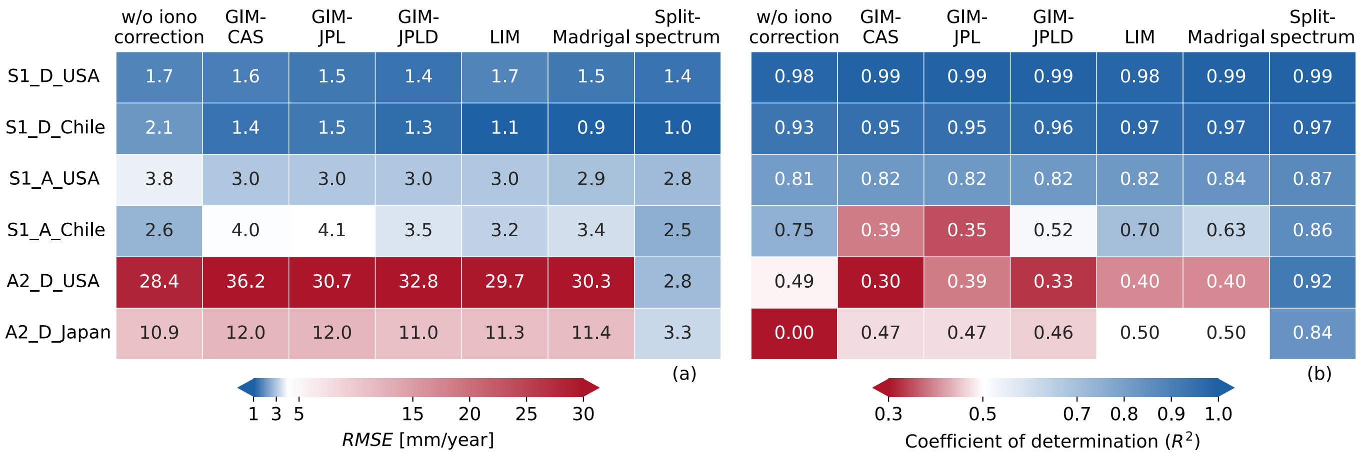

(a)

	w/o iono correction	GIM-CAS	GIM-JPL	GIM-JPLD	LIM	Madrigal	Split-spectrum
S1_D_USA	1.7	1.6	1.5	1.4	1.7	1.5	1.4
S1_D_Chile	2.1	1.4	1.5	1.3	1.1	0.9	1.0
S1_A_USA	3.8	3.0	3.0	3.0	3.0	2.9	2.8
S1_A_Chile	2.6	4.0	4.1	3.5	3.2	3.4	2.5
A2_D_USA	28.4	36.2	30.7	32.8	29.7	30.3	2.8
A2_D_Japan	10.9	12.0	12.0	11.0	11.3	11.4	3.3

(b)

	w/o iono correction	GIM-CAS	GIM-JPL	GIM-JPLD	LIM	Madrigal	Split-spectrum
S1_D_USA	0.98	0.99	0.99	0.99	0.98	0.99	0.99
S1_D_Chile	0.93	0.95	0.95	0.96	0.97	0.97	0.97
S1_A_USA	0.81	0.82	0.82	0.82	0.82	0.84	0.87
S1_A_Chile	0.75	0.39	0.35	0.52	0.70	0.63	0.86
A2_D_USA	0.49	0.30	0.39	0.33	0.40	0.40	0.92
A2_D_Japan	0.00	0.47	0.47	0.46	0.50	0.50	0.84

Fig. 9. (a) RMSE and (b) R^2 results of InSAR and GNSS deformation velocity for different ionospheric correction methods across all Sentinel-1 and ALOS-2 tracks. The darker the blue color, the better the InSAR performance; the darker the red color, the greater the discrepancy between InSAR and GNSS.

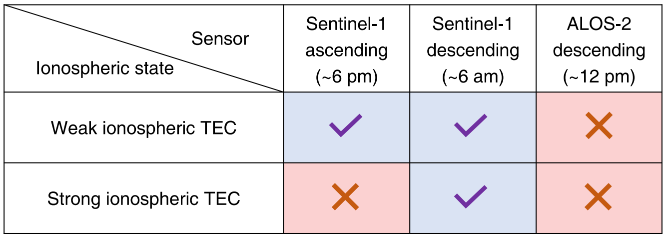

Sensor / Ionospheric state	Sentinel-1 ascending (~6 pm)	Sentinel-1 descending (~6 am)	ALOS-2 descending (~12 pm)
Weak ionospheric TEC	✓	✓	✗
Strong ionospheric TEC	✗	✓	✗

Fig. 10. Summary of long-wavelength ionospheric correction for InSAR time series using GNSS-based TEC products.

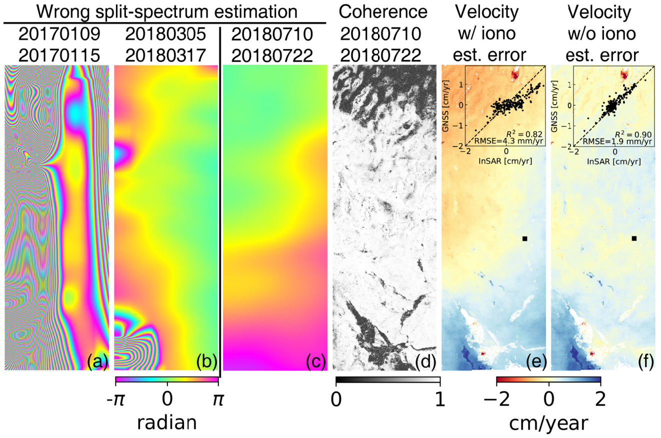

Fig. 11. Examples of inaccurate ionospheric delay phase estimations from the range split-spectrum method. (a) and (b) Sentinel-1 ascending track 064 using SLCs acquired between January 9–15, 2017, and between March 5–17, 2018, respectively. (c) Sentinel-1 ascending track 166 using SLCs acquired between July 10–22, 2018. (d) Spatial coherence of the regular interferogram for (c). (e) Ionosphere-corrected velocity after excluding range split-spectrum estimation error types of (a) and (b). (f) Similar to (e) but after excluding range split-spectrum estimation error types of (a)–(c). Scatter plots in (e) and (f) show the comparison between GNSS and InSAR with reference point in GNSS station NVSL. Similar to Fig. 6, a Heaviside step function is used to account for the impact of the 2019 Ridgecrest earthquakes.

deformation velocity derived from InSAR, as demonstrated by the comparison between Fig. 11(e) and (f), with the latter showing improved consistency with GNSS observations. More specifically, the RMSE changes from 4.3 to 1.9 mm/yr. These findings highlight the strong dependence of conventional approaches on both coherence and manual inspection, indicating that ionospheric phase selection should not rely solely on phase consistency but must also incorporate coherence information.

B. Ionospheric Correction of OPERA Displacement Products

The OPERA Level-3 surface displacement (OPERA-DISP) product [71], [72], a time-series dataset from Sentinel-1, provides wide-area coverage. We incorporate Madrigal TEC products into the latest OPERA-DISP dataset, applying ionospheric corrections over six ascending tracks in the western USA, to validate the feasibility of our proposed method for the OPERA-DISP dataset. For computational efficiency over large-scale regions, we multilook with ten looks in both range and azimuth directions. MintPy is then used to correct for troposphere and solid Earth tides following the procedure described in Section III, and the deformation velocity fields are subsequently derived. Each frame is processed independently, after which frames are mosaicked by first stitching frames within each track and then merging across tracks. During mosaicking, the median values in overlapping areas are subtracted to ensure consistency.

The results are shown in Fig. 12. Among the six tracks, the three on the left use data spanning 2016–2024, whereas the three on the right are based on data from 2016 to 2021. Due to the temporal inconsistency, notable differences are observed in the apparent ionospheric velocity [12]. After applying ionospheric correction with Madrigal TEC products, the RMSE between InSAR and GNSS velocity is reduced from 3.8 to 2.8 mm/yr, corresponding to a 26% improvement. The correction performance is comparable to that achieved using the range split-spectrum method for the Sentinel-1 ascending tracks in the western USA [see Fig. 6 (g)], confirming the feasibility of GNSS-based TEC method for OPERA-DISP ionospheric correction for long wavelength deformation mapping.

C. Accuracy Evaluation of GNSS-Based TEC Gradients

In this discussion, we assess the accuracy of north–south and east–west ionospheric gradients derived from different GNSS-based TEC products [see Fig. 13(j) and (k)], using

TABLE III

ACCURACY OF NORTH–SOUTH AND EAST–WEST GRADIENTS OF VARIOUS GNSS-BASED TEC PRODUCTS

Track	Local solar time	Band	East-West TEC gradient [TECU/100km] GIM-CAS	GIM-JPL	GIM-JPLD	LIM	Madrigal	North-South TEC gradient [TECU/100km] GIM-CAS	GIM-JPL	GIM-JPLD	LIM	Madrigal
S1_D_USA	~6 am	C	0.41	0.41	0.40	0.41	0.37	0.29	0.29	0.26	0.29	0.25
S1_D_Chile	~6 am	C	0.49	0.49	0.47	0.49	0.47	0.27	0.23	0.27	0.20	0.20
S1_A_USA	~6 pm	C	0.47	0.44	0.43	0.47	0.41	0.25	0.26	0.25	0.25	0.24
S1_A_Chile	~6 pm	C	2.48	2.53	2.53	2.48	2.54	2.02	2.02	2.00	1.87	2.00
A2_D_USA	~12 pm	L	1.03	1.03	1.01	1.02	1.02	0.25	0.26	0.20	0.23	0.22
A2_D_Japan	~12 pm	L	1.26	1.25	1.25	1.20	1.23	0.41	0.39	0.35	0.36	0.35

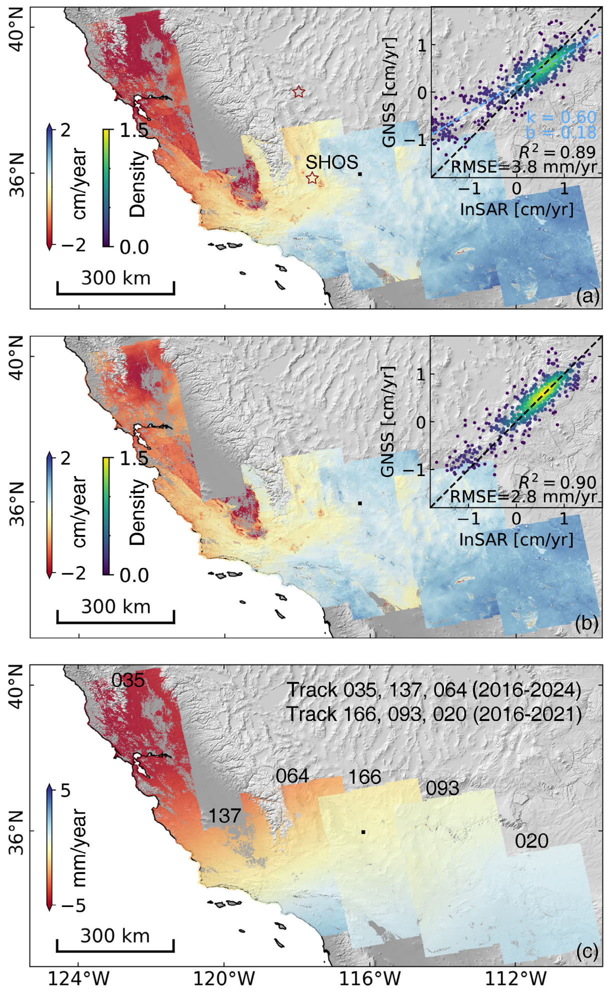

Fig. 12. Ionospheric correction of the OPERA Level-3 surface displacement from Sentinel-1 using Madrigal TEC products [(left to right) tracks 035, 137, 064, 166, 093, and 020]. (a) LOS velocity before ionosphere correction, with a linear fit (blue line) yielding $v_{\text{GNSS}} = 0.6\, v_{\text{InSAR}} + 0.18$. (b) LOS velocity after ionospheric correction using Madrigal TEC products. (c) Apparent ionospheric velocity from Madrigal TEC products. Black points represent reference points in GNSS station SHOS. Scatter plot in (a) and (b) comparison between InSAR and 758 GNSS stations. Similar to Fig. 6, a Heaviside step function is used to account for the impact of the 2019 Ridgecrest earthquakes.

ionospheric delays estimated with the range split-spectrum method as the reference. The results demonstrate that the performance of these products is generally comparable under relatively quiet solar conditions [see Fig. 13(a)–(d)], but exhibits instability during active solar conditions [see Fig. 13(e)–(h)].

To quantify the differences, we analyze the ionospheric delay phase time series. For each acquisition time, we estimate the phase ramp of the ionospheric delay and convert it into north–south and east–west gradients [see Fig. 13(a)]. The RMSE between the ionospheric delays estimated from the time series and those obtained with the range split-spectrum method is then calculated, and the gradient accuracy is summarized in Table III. Specifically, under low TEC conditions (6 A.M. at low latitudes and 6 A.M./P.M. at mid-latitudes, mean TEC of ~11 TECU), the east–west and north–south gradient accuracies are 0.37–0.49 and 0.20–0.29 TECU/100 km, respectively. Under moderate TEC conditions (12 P.M. at mid-latitudes, mean TEC of ~15 TECU), the east–west and north–south gradient accuracies are 1.01–1.26 and 0.20–0.41 TECU/100 km, respectively. Under high TEC conditions (6 P.M. at low latitudes, mean TEC of 20 + TECU), the east–west and north–south gradient accuracies are 2.48–2.54 and 1.87–2.02 TECU/100 km, respectively. Overall, the results demonstrate that GNSS-based TEC products provide more reliable gradient estimates in the north–south direction than in the east–west direction, and the estimation achieves higher accuracy under low TEC conditions.

D. Accuracy Evaluation of Smartphone-Based TEC Gradients

We test the newly developed smartphone-based TEC products from Google [42], derived from approximately 40 million smartphones with a spatial resolution of 0.43°–1° in latitude and 0.6°–1° in longitude, and a temporal resolution of 10 min. Using C-band Sentinel-1 track 064 data, we estimate the ionospheric delay time series over the western USA. We first converted its native S2 geospatial indexing system into a 1° × 1° latitude–longitude grid, then applied the filtering strategy illustrated in Section II to smooth the data, and next computed the ionospheric delay time series. Fig. 14 shows the east–west and north–south TEC gradient time series, similar to Fig. 13(j) and (k). Compared with the Madrigal TEC, the smartphone-based TEC performs worse in the east–west direction, but better in the north–south direction. However, this product has not been operationally generated

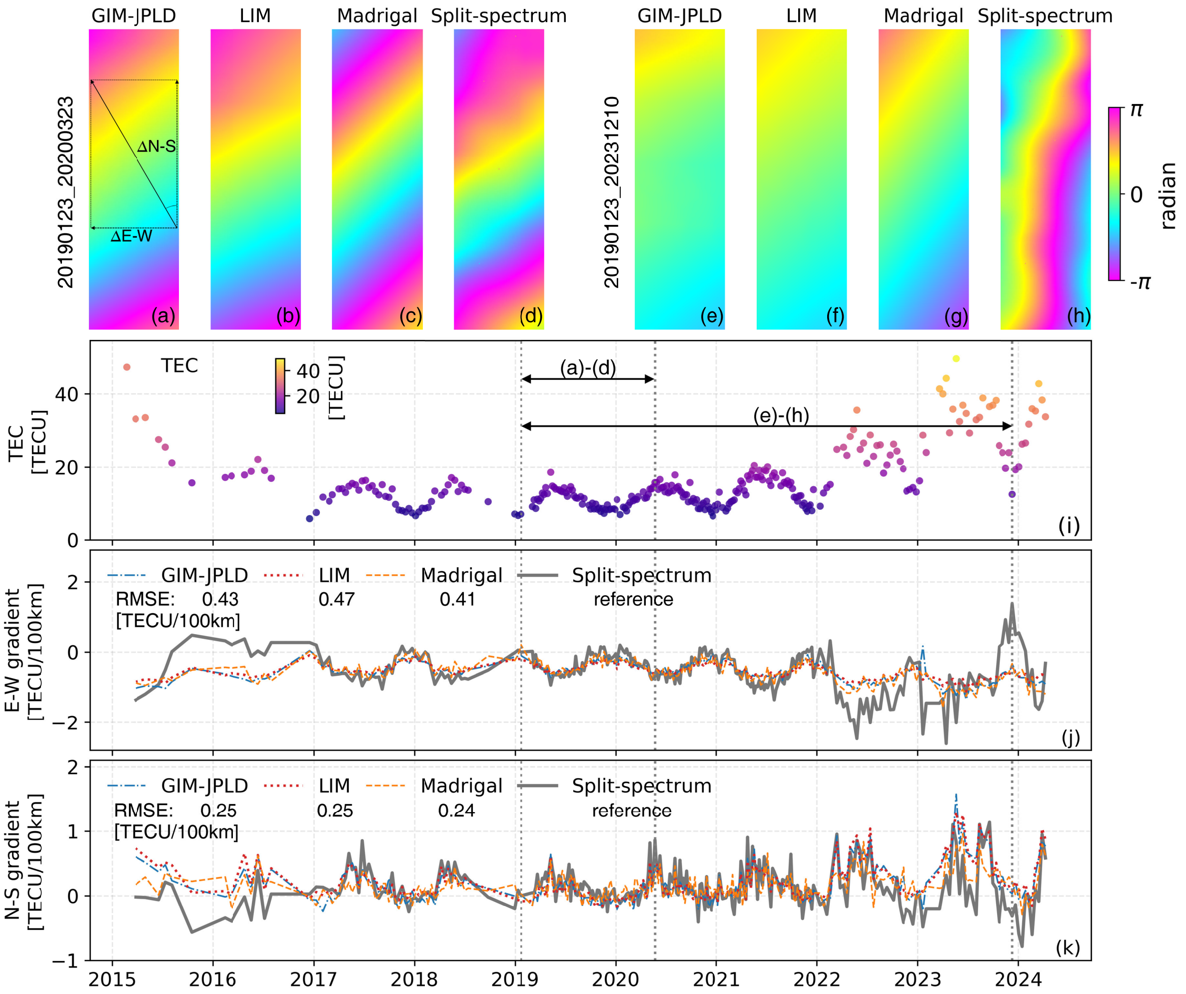

Fig. 13. TEC gradient accuracy of GIM-JPLD, LIM, and Madrigal TEC products for Sentinel-1 ascending track 064. (a)–(d) Ionospheric phase estimation between January 23, 2019 and May 23, 2020 from various methods, which are used to estimate the linear phase gradient. (e)–(h) Similar to (a)–(d) but for January 23, 2019 and December 10, 2023. (i) Absolute TEC time series at scene center from GIM-JPLD. (j) Comparison among east–west ionospheric gradient time series estimated from GIM-JPLD, LIM, Madrigal TEC, and range split-spectrum, respectively. The RMSE is calculated for each GNSS-based TEC product using the range split-spectrum as reference. Each GNSS-based TEC gradient time series is shifted by its median difference with the reference. (k) Similar to (j) but in the north–south direction.

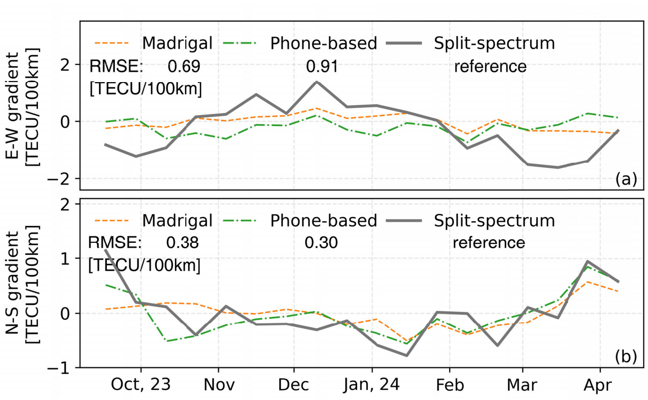

Fig. 14. TEC gradient time series. (a) and (b) Similar to Fig. 13(j) and (k), but for Madrigal and smartphone-based TEC products.

and released yet, thus, it can not be applied to our time series datasets with its current temporal coverage of September 2023 to May 2024.

E. Global Apparent Ionospheric InSAR Velocity Gradient

To analyze the spatial distribution of global ionospheric delay change velocity, we use GIM-JPLD data from 2019 (last solar minimum) to 2025 (solar maximum) to calculate the daily ionospheric delay for L-band and C-band at 6 A.M./P.M. and 12 A.M./P.M. local solar time using equations (1) and (2). We then estimate the apparent ionospheric delay velocity gradient along the north–south and east–west directions (see Fig. 15), with a fixed incident angle of 42° and orbital inclination of 98.4°.

Temporally, among the four selected times, the ionospheric delay velocity is strongest at 6 P.M., also high at 12 A.M./P.M., and weakest at 6 A.M., when the ionosphere is relatively quiet. Spatially, the north–south velocity gradient exhibits more significant variations than the east–west gradient. Regions strongly affected by ionospheric delays include central America, northern South America, central and northern Africa, the Middle East, South Asia, Southeast Asia, and southern East Asia. For SAR missions, descending tracks of

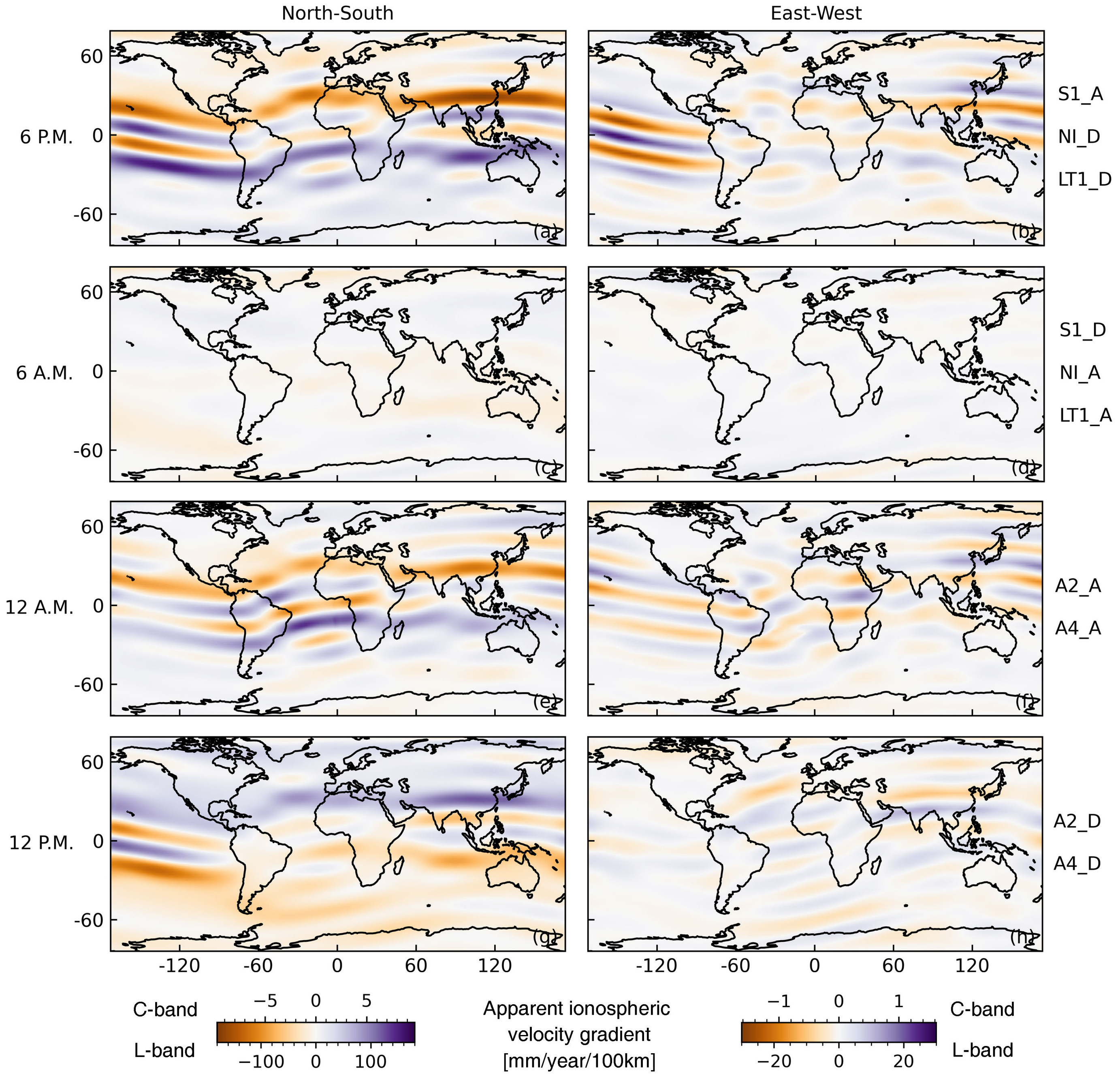

Fig. 15. Global apparent ionospheric velocity gradients in the (left) north–south and (right) east–west directions for SAR systems in sun-synchronous orbits at C-/L-band during the last half solar cycle (2019–2025) based on GIM-JPLD data. A fixed incident angle of 42° with the orbital inclination of 98.4° is used for the calculation. (a) and (b) 6 P.M., (c) and (d) 6 A.M., (e) and (f) 12 A.M., (g) and (h) 12 P.M. local solar time, respectively, roughly covering the local solar time for Sentinel-1, NISAR, LuTan-1, ALOS-2, and ALOS-4.

NISAR and LuTan-1, ascending tracks of Sentinel-1, and both ascending and descending tracks of ALOS-2/4 are expected to be strongly influenced by ionospheric delay velocities, requiring special attention. Regarding frequency dependence, the ionospheric impact at L-band is approximately 17 times stronger than at C-band [35]. Overall, this dataset provides valuable references for assessing ionospheric activity for InSAR studies.

F. Limitations of the GNSS-Based TEC Approach

The GNSS-based TEC approach is robust and computationally very efficient, making it desirable for operational data systems, large-scale deformation mapping, and areas with strong decorrelation. However, several limitations should be acknowledged. First, its accuracy is limited by the spatial distribution of the GNSS data [47] and by modeling uncertainties. In regions with insufficient GNSS coverage, such as northern Africa, northern South America, and central Asia, the performance of this approach degrades significantly and may even become infeasible. Second, due to the coarse spatial and temporal resolution of existing GNSS-based TEC products, the proposed method is primarily effective for long-wavelength ionospheric correction, whereas short-wavelength distortions still require compensation using the range split-spectrum or other SAR-derived techniques. On the other hand, the range split-spectrum method provides higher accuracy and resolution in highly coherent areas, but demands greater computational resources and performs less effectively in regions with severe decorrelation. Therefore, the two methods are complementary, and the GNSS-based TEC method could serve as a simple basis for rapid ionospheric correction.

V. CONCLUSION

We evaluate the feasibility of long-wavelength ionospheric correction for InSAR time series using GNSS-based TEC products. We test this approach on C-band Sentinel-1 and L-band ALOS-2 data over three different regions and find that: 1) for all C-band Sentinel-1 descending tracks and ascending tracks in mid-latitude regions, the GNSS-based TEC correction is effective and reduces the RMSE from 1.7–3.8 to 0.9–2.9 mm/yr, which is comparable to the well-established range split-spectrum method (1.0–2.8 mm/yr) and 2) for C-band Sentinel-1 ascending tracks in low-latitude regions with strong ionospheric disturbances and all L-band ALOS-2 data, the GNSS-based TEC correction does not work, while the range split-spectrum method remains the same level of accuracy (2.8–3.3 mm/year).

All five GNSS-based TEC products show more accurate TEC gradients in the north–south direction than in the east–west direction, and are more accurate under weak ionospheric conditions. Among the five TEC products examined, the Madrigal TEC, LIM, and GIM-JPLD exhibit better performance than the other TEC products. A global analysis of the apparent ionospheric velocity based on the GIM-JPLD highlights regions strongly affected by ionospheric disturbances, including central America, central and northern South America and Africa, Middle East, and southern and southeast Asia.

This work demonstrates the potential of GNSS-based TEC correction as a rapid and robust solution for long-wavelength ionospheric correction in InSAR time series. To evolve into a more accurate correction method, future research and development should be devoted to the mesoscale detail-preserving interpolation of the high-resolution TEC products, the integration of local and single GNSS observations into the global ionospheric products, and the operational ionospheric products from smartphones.

DATA AND CODE AVAILABILITY

The global daily ionospheric delay product is available at https://doi.org/10.5281/zenodo.17639765. The ionospheric delay calculation code is implemented in Python and available at https://doi.org/10.5281/zenodo.17172745

ACKNOWLEDGMENT

The Sentinel-1 data were provided by ESA and obtained from Alaska Satellite Facility via the Seamless SAR Archive (SSARA), a service provided by the EarthScope Consortium. The ALOS-2 data were provided by Japan Aerospace Exploration Agency (JAXA). The authors would like to thank Changyang Hu and Qingyue Yang for discussions.

REFERENCES

[1] M. Simons and P. A. Rosen, *3.12—Interferometric Synthetic Aperture Radar Geodesy*(Treatise on Geophysics), vol. 3, 2nded., Amsterdam, The Netherlands: Elsevier, 2015, pp. 339–385, doi: 10.1016/B978-0-444-53802-4.00061-0.

[2] L. Xu et al., "The overall-subshear and multi-segment rupture of the 2023 Mw7.8 Kahramanmaraş, Turkey earthquake in millennia supercycle," *Commun. Earth Environ.*, vol. 4, no. 1, p. 379, Oct.2023, doi: 10.1038/s43247-023-01030-x.

[3] Z. Yunjun, F. Amelung, and Y. Aoki, "Imaging the hydrothermal system of kirishima volcanic complex with L-band InSAR time series," *Geophys. Res. Lett.*, vol. 48, no. 11, Jun.2021, Art. no. e2021GL092879, doi: 10.1029/2021gl092879.

[4] X. Liu et al., "Integration of Sentinel-1 and ALOS/PALSAR-2 SAR datasets for mapping active landslides along the Jinsha river corridor, China," *Eng. Geol.*, vol. 284, Apr.2021, Art. no. 106033, doi: 10.1016/j.enggeo.2021.106033.

[5] J. Tarricone, R. Palomaki, K. Rittger, A. Nolin, H.-P. Marshall, and C. Vuyovich, "Investigating the impact of optical snow cover data on L-band InSAR snow water equivalent retrievals," *J. Remote Sens.*, vol. 5, p. 0682, Jan.2025, doi: 10.34133/remotesensing.0682.

[6] F. Amelung, D. L. Galloway, J. W. Bell, H. A. Zebker, and R. J. Laczniak, "Sensing the ups and Downs of las vegas: InSAR reveals structural control of land subsidence and aquifer-system deformation," *Geology*, vol. 27, no. 6, p. 483, 1999, doi: 10.1130/0091-7613(1999)027\%3C0483:STUADO\%3E2.3.CO;2.

[7] H. A. Zebker and J. Villasenor, "Decorrelation in interferometric radar echoes," *IEEE Trans. Geosci. Remote Sens.*, vol. 30, no. 5, pp. 950–959, May1992, doi: 10.1109/36.175330.

[8] Z. Yunjun, H. Fattahi, and F. Amelung, "Small baseline InSAR time series analysis: Unwrapping error correction and noise reduction," *Comput. Geosci.*, vol. 133, Dec.2019, Art. no. 104331, doi: 10.1016/j.cageo.2019.104331.

[9] H. Rishbeth and O. K. Garriott, *Introduction To Ionospheric Physics (International Geophysics)*, vol. 14. New York, NY, USA: Academic, 1969.

[10] O. Witasse et al., "Solar system ionospheres," *Space Sci. Rev.*, vol. 139, nos. 1–4, pp. 235–265, Aug.2008, doi: 10.1007/s11214-008-9395-3.

[11] O. L. Stephenson, Y.-K. Liu, Z. Yunjun, M. Simons, P. Rosen, and X. Xu, "The impact of plate motions on long-wavelength InSAR-derived velocity fields," *Geophys. Res. Lett.*, vol. 49, no. 21, Nov.2022, Art. no. e2022GL099835, doi: 10.1029/2022gl099835.

[12] Y.-K. Liu, Z. Yunjun, and M. Simons, "Inferring tectonic plate rotations from InSAR time series," *Geophys. Res. Lett.*, vol. 52, no. 12, Jun.2025, Art. no. e2025GL115137, doi: 10.1029/2025gl115137.

[13] A. Freeman, "Calibration of linearly polarized polarimetric SAR data subject to Faraday rotation," *IEEE Trans. Geosci. Remote Sens.*, vol. 42, no. 8, pp. 1617–1624, Aug.2004, doi: 10.1109/TGRS.2004.830161.

[14] F. J. Meyer and J. B. Nicoll, "Prediction, detection, and correction of Faraday rotation in full-polarimetric L-band SAR data," *IEEE Trans. Geosci. Remote Sens.*, vol. 46, no. 10, pp. 3076–3086, Oct.2008.

[15] S. Mancon, D. Giudici, and S. Tebaldini, "The ionospheric effects mitigation in the BIOMASS mission exploiting multi-squint coherence supported by Faraday rotation," in *Proc. 12th Eur. Conf. Synth. Aperture Radar*, Jun. 2018, pp. 1–6.

[16] F. Meyer, R. Bamler, N. Jakowski, and T. Fritz, "The potential of low-frequency SAR systems for mapping ionospheric TEC distributions," *IEEE Geosci. Remote Sens. Lett.*, vol. 3, no. 4, pp. 560–564, Oct.2006, doi: 10.1109/LGRS.2006.882148.

[17] R. Brcic, A. Parizzi, M. Eineder, R. Bamler, and F. Meyer, "Estimation and compensation of ionospheric delay for SAR interferometry," in *Proc. IEEE Int. Geosci. Remote Sens. Symp.*, Jul. 2010, pp. 2908–2911, doi: 10.1109/IGARSS.2010.5652231.

[18] N. B. D. Bechor and H. A. Zebker, "Measuring two-dimensional movements using a single InSAR pair," *Geophys. Res. Lett.*, vol. 33, no. 16, Aug.2006, Art. no. L16311, doi: 10.1029/2006gl026883.

[19] H.-S. Jung, D.-T. Lee, Z. Lu, and J.-S. Won, "Ionospheric correction of SAR interferograms by multiple-aperture interferometry," *IEEE Trans. Geosci. Remote Sens.*, vol. 51, no. 5, pp. 3191–3199, May2013, doi: 10.1109/TGRS.2012.2218660.

[20] P. A. Rosen, S. Hensley, and C. Chen, "Measurement and mitigation of the ionosphere in L-band interferometric SAR data," in *Proc. IEEE Radar Conf.*, May 2010, pp. 1459–1463, doi: 10.1109/RADAR.2010.5494385.

[21] G. Gomba, A. Parizzi, F. De Zan, M. Eineder, and R. Bamler, "Toward operational compensation of ionospheric effects in SAR interferograms: The split-spectrum method," *IEEE Trans. Geosci. Remote Sens.*, vol. 54, no. 3, pp. 1446–1461, Mar.2016, doi: 10.1109/TGRS.2015.2481079.

[22] H. Fattahi, P. Agram, and M. Simons, "A network-based enhanced spectral diversity approach for TOPS time-series analysis," *IEEE Trans. Geosci. Remote Sens.*, vol. 55, no. 2, pp. 777–786, Feb.2017, doi: 10.1109/TGRS.2016.2614925.

[23] G. Gomba and F. De Zan, "Bayesian data combination for the estimation of ionospheric effects in SAR interferograms," *IEEE Trans. Geosci. Remote Sens.*, vol. 55, no. 11, pp. 6582–6593, Nov.2017, doi: 10.1109/TGRS.2017.2730438.

[24] G. Gomba, F. Rodríguez González, and F. De Zan, "Ionospheric phase screen compensation for the Sentinel-1 TOPS and ALOS-2 ScanSAR modes," *IEEE Trans. Geosci. Remote Sens.*, vol. 55, no. 1, pp. 223–235, Jan.2017, doi: 10.1109/TGRS.2016.2604461.

[25] C. Liang, Z. Liu, E. J. Fielding, and R. Bürgmann, "InSAR time series analysis of L-band wide-swath SAR data acquired by ALOS-2," *IEEE Trans. Geosci. Remote Sens.*, vol. 56, no. 8, pp. 4492–4506, Aug.2018, doi: 10.1109/TGRS.2018.2821150.

[26] C. Liang, P. Agram, M. Simons, and E. J. Fielding, "Ionospheric correction of InSAR time series analysis of C-band Sentinel-1 TOPS data," *IEEE Trans. Geosci. Remote Sens.*, vol. 57, no. 9, pp. 6755–6773, Sep.2019, doi: 10.1109/TGRS.2019.2908494.

[27] A. J. Coster, E. M. Gaposchkin, and L. E. Thornton, "Real-time ionospheric monitoring system using GPS," *Navigation*, vol. 39, no. 2, pp. 191–204, Jun.1992, doi: 10.1002/j.2161-4296.1992.tb01874.x.

[28] M. Costantini et al., "European ground motion service (EGMS)," in *Proc. IEEE Int. Geosci. Remote Sens. Symp. IGARSS*, Jul. 2021, pp. 3293–3296, doi: 10.1109/IGARSS47720.2021.9553562.

[29] H. Fattahi, "Monitoring the dynamics of Earth surface with the national and global NASA's SAR products from NISAR and Sentinel-1," in *Proc. AGU Fall Meeting*, 2023, Paper G21A-01, doi: 10.48577/jpl.XAIJWG.

[30] M. Lazecký et al., "LiCSAR: An automatic InSAR tool for measuring and monitoring tectonic and volcanic activity," *Remote Sens.*, vol. 12, no. 15, p. 2430, Jul.2020, doi: 10.3390/rs12152430.

[31] D. P. S. Bekaert et al., "Development and dissemination of standardized geodetic products by the advanced rapid imaging and analysis (ARIA) center for natural hazards," in *Proc. Int. Union Geodesy Geophys. (IUGG)*, 2019, Paper G23A-04.

[32] Y. Reuveni, Y. Bock, X. Tong, and A. W. Moore, "Calibrating interferometric synthetic aperture radar (InSAR) images with regional GPS network atmosphere models," *Geophys. J. Int.*, vol. 202, no. 3, pp. 2106–2119, Jul.2015, doi: 10.1093/gji/ggv253.

[33] A. J. Mannucci, B. D. Wilson, D. N. Yuan, C. H. Ho, U. J. Lindqwister, and T. F. Runge, "A global mapping technique for GPS-derived ionospheric total electron content measurements," *Radio Sci.*, vol. 33, no. 3, pp. 565–582, May1998, doi: 10.1029/97RS02707.

[34] M. Hernández-Pajares, D. Roma-Dollase, A. Krankowski, A. García-Rigo, and R. Orús-Pérez, "Methodology and consistency of slant and vertical assessments for ionospheric electron content models," *J. Geodesy*, vol. 91, no. 12, pp. 1405–1414, Dec.2017, doi: 10.1007/s00190-017-1032-z.

[35] Z. Yunjun et al., "Range geolocation accuracy of C-/L-band SAR and its implications for operational stack coregistration," *IEEE Trans. Geosci. Remote Sens.*, vol. 60, 2022, Art. no. 5227219, doi: 10.1109/TGRS.2022.3168509.

[36] H. Fattahi et al., "OPERA coregistered single look complex products from Sentinel-1 data," in *Proc. AGU Fall Meeting*, 2022, Paper G45A-03, doi: 10.48577/jpl.4ZPEJL.

[37] H. Fattahi, V. Brancato, and S. Jeong. (Jun.2024).*Opera Algorithm Theoretical Basis Document for Coregistered Single Look Complex From Sentinel-1 Data*. [Online]. Available: cumulus.asf.earthdatacloud.nasa.gov/PUBLIC/DATA/OPERA/OPERACSLC-S1ATBDD-108752Initial2024-06-24signed.pdf

[38] J. Vierinen, A. J. Coster, W. C. Rideout, P. J. Erickson, and J. Norberg, "Statistical framework for estimating GNSS bias," *Atmos. Meas. Tech.*, vol. 9, no. 3, pp. 1303–1312, 2016, doi: 10.5194/amt-9-1303-2016.

[39] W. Rideout and K. Cariglia. (2025). *CEDAR Madrigal Database*. [Online]. Available: https://cedar.openmadrigal.org

[40] W. Rideout and A. Coster, "Automated GPS processing for global total electron content data," *GPS Solutions*, vol. 10, no. 3, pp. 219–228, Jul.1, 2006, doi: 10.1007/s10291-006-0029-5.

[41] Y. Pan, M. Jin, S. Zhang, and Y. Deng, "TEC map completion through a deep learning model: SNP-GAN," *Space Weather*, vol. 19, no. 11, Nov.2021, Art. no. e2021SW002810, doi: 10.1029/2021SW002810.

[42] J. Smith et al., "Mapping the ionosphere with millions of phones," *Nature*, vol. 635, no. 8038, pp. 365–369, Nov.2024, doi: 10.1038/s41586-024-08072-x.

[43] J. Böohm and H. Schuh, *Atmospheric Effects in Space Geodesy*, vol. 5, 1sted., Berlin, Germany: Springer, 2013, p. 234, doi: 10.1007/978-3-642-36932-2.

[44] G. E. Lanyi and T. Roth, "A comparison of mapped and measured total ionospheric electron content using global positioning system and beacon satellite observations," *Radio Sci.*, vol. 23, no. 4, pp. 483–492, Jul.1988, doi: 10.1029/RS023i004p00483.

[45] J. Chen and H. A. Zebker, "Ionospheric artifacts in simultaneous L-band InSAR and GPS observations," *IEEE Trans. Geosci. Remote Sens.*, vol. 50, no. 4, pp. 1227–1239, Apr.2012, doi: 10.1109/TGRS.2011.2164805.

[46] S. Schaer, W. Gurtner, and J. Feltens, "IONEX: The ionosphere map exchange format version 1.1," in *Proc. IGS AC Workshop*, vol. 9, Darmstadt, Germany, 1998, pp. 233–247.

[47] M. Hernández-Pajares et al., "The IGS VTEC maps: A reliable source of ionospheric information since 1998," *J. Geodesy*, vol. 83, nos. 3–4, pp. 263–275, Mar.2009, doi: 10.1007/s00190-008-0266-1.

[48] Z. Li, Y. Yuan, N. Wang, M. Hernandez-Pajares, and X. Huo, "SHPTS: Towards a new method for generating precise global ionospheric TEC map based on spherical harmonic and generalized trigonometric series functions," *J. Geodesy*, vol. 89, no. 4, pp. 331–345, Apr.2015, doi: 10.1007/s00190-014-0778-9.

[49] A. J. Mannucci, B. Iijima, L. Sparks, X. Pi, B. Wilson, and U. Lindqwister, "Assessment of global TEC mapping using a three-dimensional electron density model," *J. Atmos. Solar-Terr. Phys.*, vol. 61, no. 16, pp. 1227–1236, Nov.1999, doi: 10.1016/s1364-6826(99)00053-x.

[50] L. Martire et al., "The JPL-GIM algorithm and products: Multi-GNSS high-rate global mapping of total electron content," *J. Geodesy*, vol. 98, no. 5, p. 44, May2024, doi: 10.1007/s00190-024-01860-3.

[51] J. M. Dow, R. E. Neilan, and C. Rizos, "The international GNSS service in a changing landscape of global navigation satellite systems," *J. Geodesy*, vol. 83, nos. 3–4, pp. 191–198, Mar.2009, doi: 10.1007/s00190-008-0300-3.

[52] E. E. Zawacki, D. J. Charlevoix, C. M. Meertens, J. T. Freymueller, and T. van Dam, "A history of UNAVCO: Four decades of advancing geodesy," *Perspect. Earth Space Scientists*, vol. 6, no. 1, Dec.2025, Art. no. e2025CN000276, doi: 10.1029/2025cn000276.

[53] J. Wang, G. Huang, P. Zhou, Y. Yang, Q. Zhang, and Y. Gao, "Advantages of uncombined precise point positioning with fixed ambiguity resolution for slant total electron content (STEC) and differential code bias (DCB) estimation," *Remote Sens.*, vol. 12, no. 2, p. 304, Jan.2020, doi: 10.3390/rs12020304.

[54] W. Li et al., "A satellite-based method for modeling ionospheric slant TEC from GNSS observations: Algorithm and validation," *GPS Solutions*, vol. 26, no. 1, p. 14, Nov.15, 2021, doi: 10.1007/s10291-021-01191-2.

[55] A. Liu, Z. Li, N. Wang, Y. Zhang, A. Krankowski, and H. Yuan, "SHAKING: Adjusted spherical harmonics adding KrigING method for near real-time ionospheric modeling with multi-GNSS observations," *Adv. Space Res.*, vol. 71, no. 1, pp. 67–79, Jan.2023, doi: 10.1016/j.asr.2022.07.049.

[56] T. Sadeghi Chorsi, J. Braunmiller, F. Deng, and T. H. Dixon, "Afterslip from the 2020 M 6.5 Monte Cristo range, Nevada earthquake," *Geophys. Res. Lett.*, vol. 49, no. 17, Sep.2022, Art. no. e2022GL099952, doi: 10.1029/2022gl099952.

[57] X. Xu et al., "Surface deformation associated with fractures near the 2019 ridgecrest earthquake sequence," *Science*, vol. 370, no. 6516, pp. 605–608, Oct.2020, doi: 10.1126/science.abd1690.

[58] H. Yue et al., "The 2016 Kumamoto mw = 7.0 earthquake: A significant event in a fault–Volcano system," *J. Geophys. Res., Solid Earth*, vol. 122, no. 11, pp. 9166–9183, Nov.2017, doi: 10.1002/2017jb014525.

[59] C. Liang and E. J. Fielding, "Interferometry with ALOS-2 full-aperture ScanSAR data," *IEEE Trans. Geosci. Remote Sens.*, vol. 55, no. 5, pp. 2739–2750, May2017, doi: 10.1109/TGRS.2017.2653190.

[60] P. A. Rosen, E. Gurrola, G. F. Sacco, and H. Zebker, "The InSAR scientific computing environment," in *Proc. 9th Eur. Conf. Synth. Aperture Radar*, Apr. 2012, pp. 730–733.

[61] T. G. Farr et al., "The shuttle radar topography mission," *Rev. Geophys.*, vol. 45, no. 2, Jun.2007, Art. no. RG2004, doi: 10.1029/2005rg000183.

[62] C. W. Chen and H. A. Zebker, "Two-dimensional phase unwrapping with use of statistical models for cost functions in nonlinear optimization," *J. Opt. Soc. Amer. A, Opt. Image Sci.*, vol. 18, no. 2, p. 338, Feb.2001, doi: 10.1364/josaa.18.000338.

[63] H. Hersbach et al., "The ERA5 global reanalysis," *Quart. J. Roy. Meteorological Soc.*, vol. 146, no. 730, pp. 1999–2049, Jul.2020, doi: 10.1002/qj.3803.

[64] R. Jolivet, R. Grandin, C. Lasserre, M.-P. Doin, and G. Peltzer, "Systematic InSAR tropospheric phase delay corrections from global meteorological reanalysis data," *Geophys. Res. Lett.*, vol. 38, no. 17, p. n/a, Sep.2011, doi: 10.1029/2011gl048757.

[65] H. Fattahi and F. Amelung, "DEM error correction in InSAR time series," *IEEE Trans. Geosci. Remote Sens.*, vol. 51, no. 7, pp. 4249–4259, Jul.2013, doi: 10.1109/TGRS.2012.2227761.

[66] D. Milbert. (2018). *Solid: Solid Earth Tide*. Accessed: Sep.6, 2020. [Online]. Available: https://geodesyworld.github.io/SOFTS/solid.htm

[67] G. Blewitt, W. Hammond, and C. Kreemer, "Harnessing the GPS data explosion for interdisciplinary science," *Eos*, vol. 99, Sep.2018, doi: 10.1029/2018eo104623.

[68] M. Fernández et al., "Copernicus Sentinel–1 POD reprocessing campaign," *Adv. Space Res.*, vol. 70, no. 2, pp. 249–267, Jul.2022, doi: 10.1016/j.asr.2022.04.036.

[69] K. Akiyama, H. Itoh, H. Masuda, S. Kasho, and T. Sakamoto, "Operational validation of precise orbit determination for ALOS-2," in *Proc. SpaceOps Conf.*, May 2016, p. 2521, doi: 10.2514/6.2016-2521.

[70] H. Fattahi and F. Amelung, "InSAR uncertainty due to orbital errors," *Geophys. J. Int.*, vol. 199, no. 1, pp. 549–560, Jul.2014, doi: 10.1093/gji/ggu276.

[71] *OPERA Surface Displacement From Sentinel-1 Validated Product (Version 1)*, NASA/JPL/OPERA, NASA Alaska Satell. Facility Distrib. Act. Arch. Center, Fairbanks, Alaska, USA, 2025, doi: 10.5067/SNWG/OPL3DISPS1-V1.

[72] S. Staniewicz et al., "Near-real-time InSAR phase estimation for large-scale surface displacement monitoring," 2025, *arXiv:2511.12051*.

Yidi Wang (Student Member, IEEE) received the B.S. degree in information and computing science from Nankai University, Tianjin, China, in 2023. She is currently pursuing the Ph.D. degree with the Aerospace Information Research Institute, Chinese Academy of Sciences, Beijing, China.

She is also a student at the University of Chinese Academy of Sciences, Beijing. Her research interests include time-series InSAR signal processing and error correction.

Zhang Yunjun (Member, IEEE) received the B.Eng. degree in remote sensing from Wuhan University, Wuhan, China, in 2011, the M.Sc. degree in geodesy from the University of Chinese Academy of Sciences, Beijing, China, in 2014, and the Ph.D. degree in geophysics from the University of Miami, Miami, FL, USA, in 2019.

He was a Post-Doctoral Scholar with the California Institute of Technology, Pasadena, CA, USA, where he was also involved with the OPERA project of the Jet Propulsion Laboratory, from 2019 to January 2023. Since then, he has joined the Aerospace Information Research Institute, Chinese Academy of Sciences, where he is currently a Professor of electrical engineering. His research interests include algorithm and tools development for SAR, InSAR and time series analysis, and their applications in geohazards and solid Earth geophysics.

Ningbo Wang received the Ph.D. degree in satellite geodesy from the Institute of Geodesy and Geophysics, Chinese Academy of Sciences (CAS), Beijing, China, in 2016.

From 2017 to 2019, he pursued Post-Doctoral research at the Technical University of Munich, Munich, Germany. He is currently an Associate Professor at the Aerospace Information Research Institute, CAS. He also serves as the President of the International Association of Geodesy Sub-Commission 4.3 from 2023 to 2027. His research interests comprise real-time GNSS data analysis and global ionospheric modeling with ground- and space-based geodetic observation techniques.

Dr. Wang is the Vice-Chair of the International GNSS Service Real-Time Working Group and the Chair of the International DORIS Service Near-Real-Time DORIS Data Working Group.

Runqing Liu received the B.S. degree from the University of Electronic Science and Technology of China, Chengdu, China, in 2023. He is currently pursuing the Ph.D. degree with the Aerospace Information Research Institute, Chinese Academy of Sciences, Beijing, China.

He is also a student at the University of Chinese Academy of Sciences, Beijing. His research interests include ionospheric modeling and processing, with an emphasis on improving ionospheric models and enhancing their applications in GNSS.

Cunren Liang received the B.S. degree from Shandong University of Science and Technology, Qingdao, China, in 2008, and the Ph.D. degree from Peking University, Beijing, China, in 2014.

He was a NASA Post-Doctoral Researcher Program Fellow at Jet Propulsion Laboratory (JPL), Pasadena, CA, USA, from 2015 to 2018. He was a Staff Scientist at California Institute of Technology (Caltech), Pasadena, from 2018 to 2021. He is currently an Assistant Professor at Peking University. His research interests are mainly in the field of microwave remote sensing, e.g., synthetic aperture radar (SAR) signal processing, interferometry (InSAR), microwave scattering mechanisms, and their applications in geoscience. Dr. Liang was a recipient of the NASA Group Achievement Award in 2016 and the JPL Outstanding Post-Doctoral Research Award in 2017.

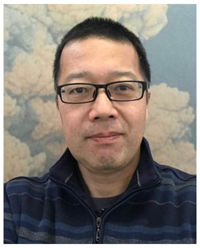

Yosuke Aoki (Member, IEEE) received the B.S., M.S., and Ph.D. degrees from the Department of Earth and Planetary Science, The University of Tokyo, Tokyo, Japan, in 1996, 1998, and 2001.

Before taking a position as a Lamont Post-Doctoral Fellow at Lamont-Doherty Earth Observatory, Columbia University, New York City, NY, USA, between 2001 and 2003, he was an Assistant Professor at Earthquake Research Institute (ERI), The University of Tokyo between 2003 and 2019, and now an Associate Professor at ERI. He is also an Adjunct Professor at the Department of Earth and Planetary Science, The University of Tokyo, and a Visiting Scientist at the RIKEN Center for Advanced Photonics. His main research interest is to measure Earth's deformation with space geodetic techniques, such as synthetic aperture radar and global navigation satellite system. He is also interested in developing physical models to explain the observed surface deformation.

Robert Wang (Senior Member, IEEE) received the B.S. degree in control engineering from the University of Henan, Kaifeng, China, in 2002, and the Dr. Eng. degree from the Graduate University of Chinese Academy of Sciences, Beijing, China, in 2007.

He was with the Center for Sensor Systems (ZESS), University of Siegen, Siegen, Germany, from 2007 to 2011, where he was involved in various joint projects supported by ZESS and Fraunhofer-FHR, Wachtberg, Germany. Since 2011, he has joined the Aerospace Information Research Institute, Chinese Academy of Sciences (CAS), Beijing, where he is currently the Director of the National Key Laboratory of Microwave Imaging and a co-Principal Investigator with the Helmholtz-CAS Joint Research Group, Beijing. He is the radar payload Principal Investigator of the LuTan-1 mission and is responsible for several high-resolution spaceborne imaging radar missions supported by the National High-Resolution Earth Observation Major Special Program. He has authored more than 100 peer-reviewed journal articles and one book. His research interests include mono-/multi-static SAR imaging and high-resolution wide-swath spaceborne SAR systems and imaging models.

Dr. Wang currently serves as an Associate Editor for the IEEE TRANSACTIONS ON GEOSCIENCE AND REMOTE SENSING.